Probing Constitutive Models of Bohus Granite with In Situ Spherical Indentation and Digital Volume Correlation

H Shariati, A Bouterf, M Saadati, P.-L Larsson, François Hild

Probing Constitutive Models of Bohus Granite with In Situ Spherical Indentation and Digital Volume Correlation

H. Shariati,[a] A. Bouterf,[b,c] M. Saadati,[d] P.-L. Larsson[a] and F. Hild[b,*]

[a]Unit of Solid Mechanics, Department of Engineering Mechanics
KTH Royal Institute of Technology, Stockholm, Sweden
[b]Université Paris-Saclay, CentraleSupélec, ENS Paris-Saclay, CNRS
LMPS–Laboratoire de Mécanique Paris-Saclay, Gif-sur-Yvette, France
[c]Now at Alpine Racing s.a.s, Viry Chatillon, France
[d]Epiroc Rock Drills AB, Örebro, Sweden
[*]Corresponding author: francois.hild@ens-paris-saclay.fr

June 26, 2022

Abstract

Spherical indentation of granite was investigated using Digital Volume Correlation (DVC) aiming at probing constitutive laws of the studied rock. *In situ* indentation was performed within an X-ray tomograph. Finite element simulations of the problem, using different constitutive models, were carried out and their trustworthiness was assessed thanks to DVC residuals. Three laws were investigated, namely, pure elasticity, then compressible elastoplasticity, and finally compressible elastoplasticity coupled with damage. Frictional contact effects were studied as well. The results show that compressible elastoplasticity should be accounted for to achieve high accuracy of results, and that frictional effects are of importance in terms of damage extent. If macrocrack initiation is also sought, then damage features should be included in the model.

Keywords

Damage; digital volume correlation (DVC); friction; granite; indentation; inelastic behavior

1 Introduction

Percussive drilling is widely used as an industrial method in which rocks are fragmented under contact loading. The mechanical problem includes spherical contact between drill bit buttons and rocks. To improve the efficiency of the drilling process, an understanding of rock failure under such conditions is required. Tkalich et al. [1] presented an experimental and numerical investigation on the response of Kuru granite under confined compression and quasi-static indentation tests with a spherical indentor. Finite element (FE) simulations (with an axisymmetric model) of static indentation were carried out by the previous authors. The influence of the material model features was discussed, and the effect of confining pressure during indentation was evaluated. The numerical simulation showed that the peak force of indentation increased with confining pressure compared to unconfined cases. Conversely, the confining pressure had a limited influence in the contact region due to high stresses induced by indentation. Based on continuum damage mechanics concepts [2], Mazars' model [3] was used to simulate the extent of the damaged zone within rocks (*i.e.,* granite, limestone and sandstone) in the vicinity of spherical drill insert during single- and double-indentation tests [4].

The inelastic behavior of Bohus granite, as prototypical of hard rocks, was experimentally and numerically investigated [5]. Several quasi-static spherical indentation tests were performed on specimens made of such material. The resulting force-penetration curves were predicted by the established compressible plasticity model, namely the Drucker-Prager law [6] with variable dilation angle. Any inelastic deformation associated with crushing at high pressures under the contact area as well as multiple microcracking were captured by such model. Then, an anisotropic damage model was added to capture mode I cracking due to tensile stress states close to the specimen surface [7]. This stress state may lead to rock cracking, and subsequently material removal on the surface. Furthermore, the frictional effects under quasi-static spherical indentation were numerically studied [8]. It was observed that the simulated force-penetration response was not affected by friction. It was also shown that the predicted fragmentation pattern was similar in both cases (*i.e.,* frictional and frictionless cases) but with a larger size in the frictional case.

One of the main challenges of indentation tests is that most of the deformation of the medium remains confined close to the zone *beneath* the indentor, which is not accessible by surface observations. Conversely, 3D imaging techniques (*e.g.,* computed tomography [9]) coupled with *in situ* tests may be considered and the deformation of the medium can then be measured by digital volume correlation (DVC) [10, 11, 12]. Such approaches then allow deformation mechanisms to be revealed and quantified, as well as constitutive models to be calibrated and/or validated. The aim of the present work is to further validate the afore-mentioned observations by performing *in situ* indentation in an X-ray scanner.

With DVC analyses, deformation mechanisms were revealed and quantified via *in situ* indentation. Cracking mechanisms were studied for indented polycrystalline alumina and it was shown that radial cracks experienced mixed mode opening displacements [12]. Compaction and cracking in plaster was analyzed thanks to micro- and nano-tomography [13]. Very early damage was observed. Pore collapse and its gradual development was detected in contrast with mesoscale studies where compaction appeared very abrupt. Deformation mechanisms of (elephant) dentin were reported [14]. The authors showed that the strain levels beneath the indentor exceeded the yield strain of dentin. The fracture development in shales was reported very recently [15]. The cracking pattern was evidenced thanks to strain fields derived from measured displacement fields. More ductile materials were also studied. Deformation mechanisms (*e.g.,* dilatancy, liquid flow, macrosegregation, and intra-granular deformation) were reported for semi-solid Al-Cu alloy [16] and for semi-solid granular alloy with an equiaxed dendritic microstructure [17]. Strain localization was quantified and the role of the underlying microstructure was highlighted.

Another route consists in the extraction of material parameters and the validation of constitutive models. Elastoplastic finite element simulations were compared to DVC measurements for ductile aluminum-silicon carbide composite (Al-SiC) [11]. Because of high strain uncertainties, computed and measured displacements were preferred and led to a good agreement. For a SiC-SiC composite, axial displacements and strains were compared with FE simulations at macroscopic and microscopic scales [18]. The damage model was qualitatively validated by using experimental and simulated axial displacements and strains. Ramberg-Osgood parameters could be extracted from an indentation test on an Al-SiC composite [19]. The difference between experimentally measured and simulated (normalized) axial displacements was minimized. Such type of analysis was extended to a nano-structured oxide dispersion strengthened steel [20]. In particular, it was shown that the effect of friction was very limited on the reported results. The compaction of glass was experimentally studied and numerically described by an approximate solution [21]. In indented plaster, a crushing criterion was proposed, calibrated thanks to indentation tests, and validated with oedometric tests [22]. Predictions with Mohr-Coulomb and crushable foam models were compared with macroscopic and microscopic data. Both models reproduced the (macroscopic) load-displacement response of the indentation test. Conversely, poor predictions of the experimental crushed zone were obtained by both models.

In the afore-mentioned studies, various DVC schemes were considered. Most of the analyses were performed with so-called local DVC [11, 12, 16, 19, 17, 18, 20, 14, 15], in which independent sub-volumes were registered. FE-based DVC was also considered, registration residuals and strain fields were utilized to characterize cracks [10, 22, 13, 21]. Furthermore, reduced bases based on elastic simulations tailored to indentation tests enabled mechanical fields (*e.g.,* stresses) to be

accessible [10, 22]. Such analyses may allow different constitutive models to be probed. In the present case, the faithfulness of elastic and two nonlinear models was probed in addition to friction via *integrated* DVC in which the selected kinematic bases included simulated displacement fields.

The paper is organized as follows. First, the spherical indentation experiment is discussed including the tomographic scans that were acquired during load application (*i.e.,in situ* test). Then, the *integrated* DVC framework is introduced. The latter was specifically tailored to the studied test. Finite element simulations were performed to construct kinematic bases for DVC analyses with different constitutive laws. Last, the integrated DVC results are presented and discussed in particular regarding the appropriateness of the three constitutive models, namely, elasticity, compressible elastoplasticity, and compressible elastoplasticity accounting for damage to describe the behavior of Bohus granite when indented by a hard material.

2 Indentation Experiment on Bohus Granite

2.1 *In Situ* Test

A cylinder (45 mm in diameter and 40 mm in height) made of Bohus granite was indented *in situ* with a 12-mm in diameter sphere made of silicon nitride (Si_3N_4). Bohus granite mainly contains quartz (33 vol%), plagioclase (32 vol%), potassium feldspar (29 vol%) and biotite (6 wt%) [23]. The sample size was chosen to enable for high resolution (*i.e.,* 30.8 µm/voxel) to be compared to the mean grain size of the order of 1 mm. The TTC testing machine of LMPS was utilized [24]. Its axial load capacity is ±20 kN (Figure 1(a)).

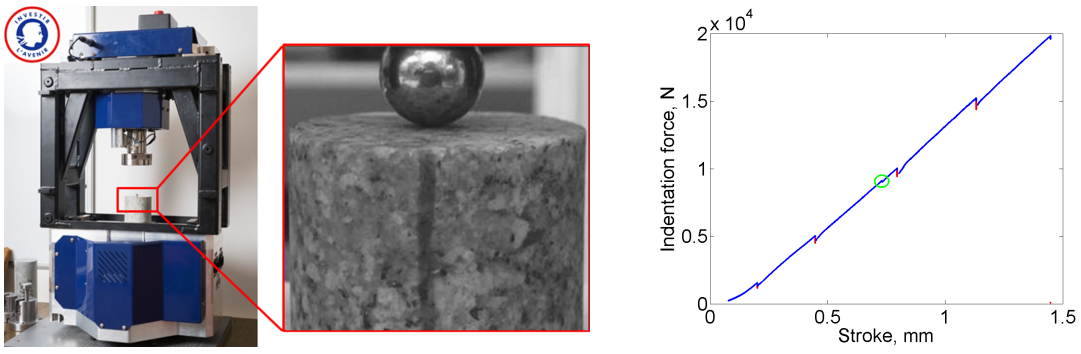

(a) (b)

Figure 1: (a) *In situ t*esting machine utilized for the reported indentation test. (b) Corresponding indentation force vs. stroke. Five tomographic acquisitions (red lines) were performed (Table 1). The green circle depicts the first drop induced by the indentation load apart from those associated with scan acquisitions

The hardware parameters of the X-ray tomograph are gathered in Appendix A. Figure 2(a)

shows a 3D rendering of the scan in the reference configuration. The indentor is clearly visible and no significant artifacts are observed around it since silicon nitride was selected. The gray level histogram of the rock is shown in Figure 2(b). Except for some very bright spots associated with most likely biotite, the contrast is rather uniformly distributed.

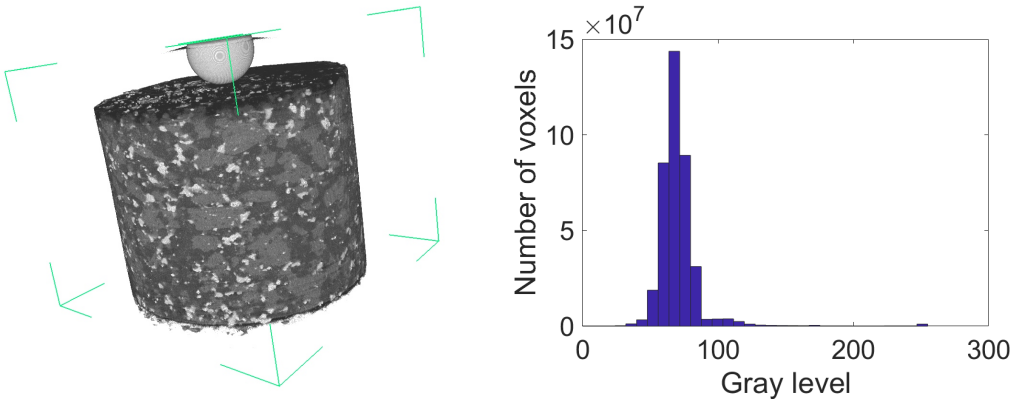

(a) (b)

Figure 2: (a) 3D rendering of the volume in the reference configuration (scan # 0). (b) Corresponding gray level histogram

After an initial scan at a pre-loaded state (Figure 1(b)), three scans were acquired for 5 kN load increments (Table 1). One scan was also acquired post-failure (*i.e.,* $F_i = 19850\ N$). Once reconstructed, the volumes prior to failure were registered via DVC analyses. In Figure 1(b), two types of load drops are observed. The first ones correspond to scan acquisitions during which small force relaxations took place. The second (green circle) was due to damage (*i.e.,* circumferential cracking) induced by the indentation load.

Table 1: Indentation force for scan acquisitions (see Figure 1(b))

Scan #	F_i (N)
0	1555
1	5025
2	10040
3	15230
4	0

2.2 Reduced Basis for DVC Analyses

In the present study, an integrated DVC framework was developed, which was specifically designed to compare different constitutive laws. It consisted in performing numerical simulations to construct reduced kinematic bases in which the displacement fields were mechanically (*i.e.,* statically

and kinematically) admissible contrary to standard DVC algorithms that do not make such hypotheses [25, 24]. For indentation experiments, reduced bases can be constructed [10]. Contrary to the afore-mentioned work that did not model the crushing zone so that boundary conditions became the unknown degrees of freedom, the volume in the close vicinity of the indentor was analyzed. Within such framework, three different scales of analysis are possible for any considered constitutive law. First, the applied force is compared to simulation results. Second, the displacement fields are computed at a scale compatible with numerical convergence. Third, the quality of the model is probed at the voxel scale thanks to the gray level residuals.

The reduced displacement basis consisted of seven fields

$$\begin{aligned}\mathbf{u}_{rbt}(t_x,t_y,t_z) &= t_x\mathbf{e}_x + t_y\mathbf{e}_y + t_z\mathbf{e}_z\\ \mathbf{u}_{rbr}(\mathbf{x},\omega_x,\omega_y,\omega_z) &= \omega_x\mathbf{r}_{yz}(y,z) + \omega_y\mathbf{r}_{zx}(x,z) + \omega_z\mathbf{r}_{xy}(x,y)\\ \mathbf{u}_{ind}(\mathbf{x},F_i,f,\mathrm{CE}) &= \mathbf{u}_{FE}(\mathbf{x},F_i,f,\mathrm{CE}) - \mathbf{u}_{FE}(\mathbf{x},F_0,f,\mathrm{CE})\end{aligned} \tag{1}$$

where $\mathbf{u}_{rbt}$ denotes the rigid body translation vector, $\mathbf{u}_{rbr}$ the displacement field induced by three rigid body rotations, and $\mathbf{u}_{ind}$ the so-called indentation displacement field. Given the fact that the first scan was acquired in a pre-loaded state (F_0), the reference configuration was not the unloaded state. Consequently, the indentation field was corrected by the displacement field computed for the corresponding indentation force F_0 (Equation (1)). In the present case, small rotations occurred, which explains the linearity with respect to the rotation amplitudes and leads to simple expressions for the corresponding fields (*e.g.,* $\mathbf{r}_{xy}(x,y) = x\mathbf{e}_y - y\mathbf{e}_x$). The fields $\mathbf{u}_{FE}$ were constructed with finite element (FE) simulations that provided results for different indentation forces F_i, friction coefficients f between the indentor and Bohus granite, and various constitutive equations (CE). In the FE simulations, the reference configuration was the load-free state.

One key parameter that is introduced hereafter allows the faithfulness of the FE simulations to be quantified. If the latter ones are fully consistent with the experiment, it should vanish. Therefore, the smaller the absolute value of this new parameter, the more trustworthy the model prediction. The seventh degree of freedom thus becomes this correction factor c that allows small offsets to the reference solution to be accounted for (*i.e.,* $(1+c)\mathbf{u}_{ind}$). The DVC analyses consisted in determining the following seven amplitudes

- three rigid body translations t_x, t_y, t_z
- three rigid body rotations $\omega_x, \omega_y, \omega_z$
- one correction factor c (at convergence)

through the minimization of the sum of squared gray level residuals over the considered region of interest (ROI)

$$\varrho^2(t_x,t_y,t_z,\omega_x,\omega_y,\omega_z,c) = \sum_{\mathrm{ROI}} \rho^2(\mathbf{x},t_x,t_y,t_z,\omega_x,\omega_y,\omega_z,c) \tag{2}$$

with

$$\rho(\mathbf{x}, t_x, t_y, t_z, \omega_x, \omega_y, \omega_z, c) = I_0(\mathbf{x}) - I_i(\mathbf{x} + \mathbf{u}_m(\mathbf{x}, t_x, t_y, t_z, \omega_x, \omega_y, \omega_z, c)) \tag{3}$$

where the measured displacement field $\mathbf{u}_m$ read

$$\mathbf{u}_m(\mathbf{x}, t_x, t_y, t_z, \omega_x, \omega_y, \omega_z, c) = \mathbf{u}_{rbt}(t_x, t_y, t_z) + \mathbf{u}_{rbt}(\mathbf{x}, \omega_x, \omega_y, \omega_z) + (1 + c)\mathbf{u}_{ind}(\mathbf{x}, F_i, f, \mathrm{CE}) \tag{4}$$

and I_0 denotes the gray level volume in the reference configuration, I_i the volumes in the deformed configurations. In the minimization scheme with respect to the sought degrees of freedom, c was not updated. Its value was only assessed at convergence so that the reference solution was probed as well as its first order deviation *at convergence for which the rigid body motions were properly accounted for.* Consequently, the predictive capacity of each model is assessed in terms of this correction factor c (*i.e.,* the closer c to zero, the better the model).

The volumes were processed using the Correli 3.0 framework [26] in which A Gauss-Newton scheme was implemented for the minimization of the sum of squared gray level residuals. The kernels of Correli 3.0 only process meshes made of 4-noded tetrahedra (T4) [27]. In the present case, the FE and DVC meshes shared the same nodes even though the interpolation hypotheses were not identical (Figure 3). The Hessian matrix $[\mathbf{H}]$ and the right hand side vectors $\{\mathbf{b}\}$ were computed with the selected discretization (Figure 3)

$$H_{ij} = \sum_{\mathrm{ROI}} \left(\boldsymbol{\nabla} I_0(\mathbf{x}) \cdot N_i(\mathbf{x})\right) \left(\boldsymbol{\nabla} I_0(\mathbf{x}) \cdot N_j(\mathbf{x})\right) \tag{5}$$

and

$$b_i = \sum_{\mathrm{ROI}} (I_0(\mathbf{x}) - I_t(\mathbf{x} + \widetilde{\mathbf{u}}(\mathbf{x})) \left(\boldsymbol{\nabla} I_0(\mathbf{x}) \cdot N_i(\mathbf{x})\right) \tag{6}$$

where $\widetilde{\mathbf{u}}$ is the current estimated of the displacement field, and $N_j(\mathbf{x})$ the vectorial shape functions. Congruential transformations were performed on the previous DVC system to account for the reduced basis in a non intrusive way. They consist in writing a master-slave transformation matrix $[\mathbf{T}]$ in which the master degrees of freedom are the seven amplitudes $\mathbf{x}, t_x, t_y, t_z, \omega_x, \omega_y, \omega_z, c$, which are gathered in the column vector $\{\mathbf{a}\}$, and the slaves are the nodal displacements of the finite element mesh (*i.e.,* column vector $\{\upsilon\}$)

$$\{\mathbf{a}\} = [\mathbf{T}]\{\upsilon\} \tag{7}$$

Each column of matrix $[\mathbf{T}]$ then corresponds to one of the seven selected displacement fields (Equation (1)). The minimization scheme then consisted in iteratively updating the amplitude corrections $\delta\{\mathbf{a}\}$ by solving linear systems

$$\left([\mathbf{T}]^\top [\mathbf{H}][\mathbf{T}]\right) \delta\{\mathbf{a}\} = [\mathbf{T}]^\top \{\mathbf{b}\} \tag{8}$$

In the present case, the correction parameter was not updated but, at convergence, it was assessed as the first order correction to be applied to the indentation field $\mathbf{u}_{ind}$. With such an implementation, the Dirichlet boundary conditions of the finite element simulations were made consistent

with the experiment, and thus the quality of the selected constitutive could be probed in terms of applied force, of its faithfulness with the correction factor c, and with gray level residuals computed for each voxel belonging to the considered ROI.

To assess $\mathbf{u}_{ind}$, FE analyses were performed using the commercial code Abaqus explicit [28]. The rock geometry was meshed with linear reduced integration (C3D8R) brick elements (Figure 3). The bottom surface of the sample was motionless. The indenter was modeled as a 3D analytical rigid surface. A vertical displacement with constant velocity was applied to the indenter. The contact force was captured by outputting the reaction force. As a result, the numerical force-penetration response could be obtained. Two contact assumptions were made, namely, frictionless and Coulomb friction with a coefficient $f = 0.4$, noting that results for intermediate frictional coefficients did not provide much effect [29]. The mesh was adapted (*i.e.,* refined) in the contact area.

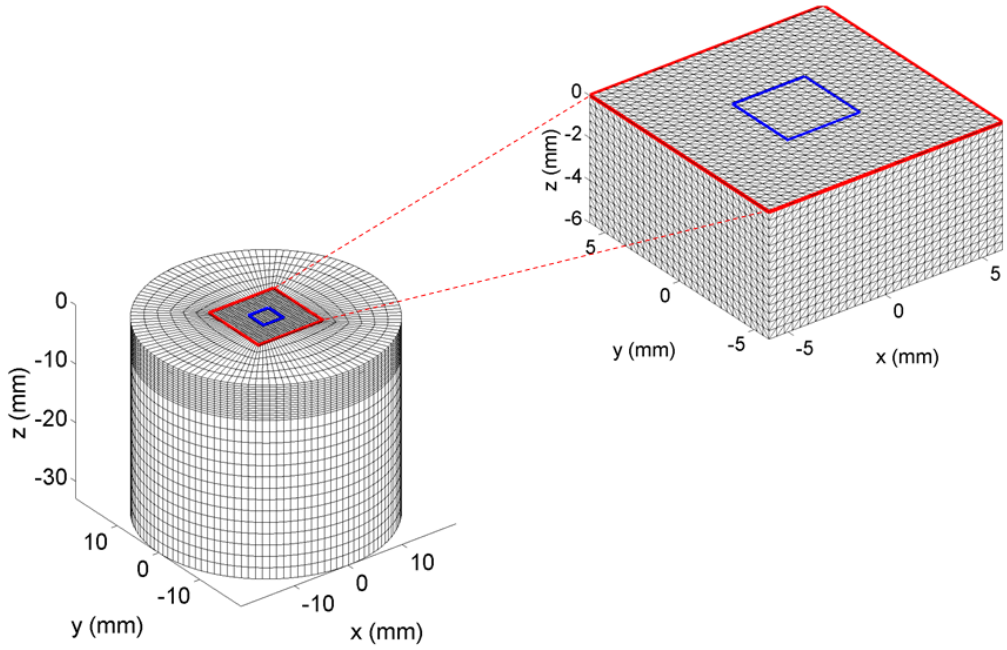

Figure 3: C3D8R mesh for numerical simulations (left) and T4 mesh (right) used for DVC analyses. The origin of the frame is located at the indentation point. The reduced ROI is such that $|x| <$ 1.85 mm, $|y| < 1.85$ mm, and $-1.85 < z < 0$ mm (see blue box)

In the most advanced constitutive equation, the Drucker-Prager law [6] was considered with variable dilation angle coupled with an anisotropic damage model [30, 31]. The constitutive equations were introduced in Abaqus explicit via a VUMAT subroutine [31]. Additional details of such FE analyses can be found in Ref. [8]. In the following analyses, the present model, which accounts for two different inelastic mechanisms, will be compared to predictions with the elastoplastic part (*i.e.,* with no damage), and an elastic Ansatz. The parameters of the three constitutive models are

gathered in Table 2. The elastic (E), elastoplastic (EP), and elastoplastic coupled with damage (EPD) models are detailed in Appendix B.

Table 2: Material parameters for the three selected models

Model	E[1]	EP[2]	EPD[3] ($f = 0$)	EPD[4] ($f = 0.4$)
Young's modulus, E (GPa)	52	52	52	52
Poisson's ratio, ν	0.25	0.25	0.25	0.25
Mass density (kg/m^3)	2630	2630	2630	2630
Cohesion, d (MPa)		153	153	153
Friction angle, β (°)		51.7	51.7	51.7
Dilation angle, ψ		see Eq. (13)	see Eq. (13)	see Eq. (13)
Weibull modulus, m			24	12
Mean failure stress, $\overline{\sigma}_F$ (MPa)			120	75
Effective volume, V_{eff} (mm^3)			1	2

[1]after Ref. [32], [2]after Refs. [32, 5], [3]after Ref. [7], [4]after Ref. [8]

Figure 4 shows the displacement fields u_z (in the axial direction) for the elastoplastic predictions when damage was included (EPD). Most of the deformation concentrates around the indentation point. The maximum amplitude is about 90 µm (or 3 vx) for the first scan, 160 µm (or 5.3 vx) for the second scan, and 220 µm (or 7.3 vx) for the third scan. Such levels are compatible with DVC analyses and validate the selected resolution (*i.e.,* 30.8 µm per vx).

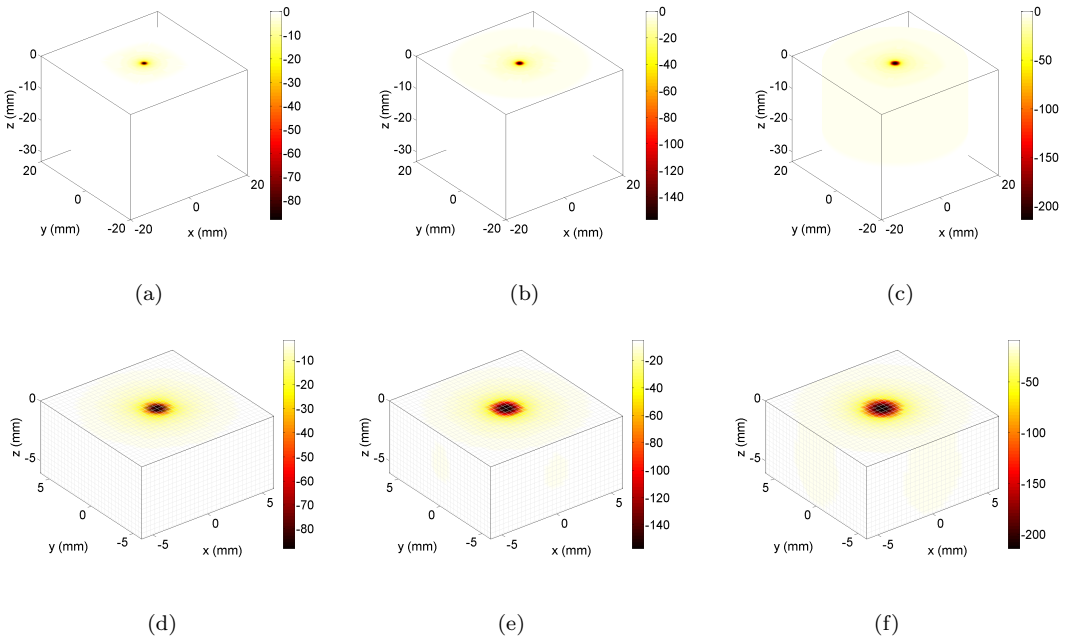

Figure 4: Axial displacement fields u_z (expressed in µm) predicted by the elastoplastic model for the three scans. Top row: complete FE model, bottom row: DVC ROI (see Figure 3). (a,d) Scan #1, (b,e) Scan #2, (c,f) Scan #3

Table 3 gathers the DVC parameters utilized in the following analyses. The element size, which is defined as the cube root of the volume of each element was equal to 7 vx (or 220 µm).

Table 3: DVC analysis parameters

DVC software	Correli 3.0 [26]
Image filtering	none
Element length (mean)	7 vx (220 µm)
Shape functions	linear (T4)
Mesh	see Figure 3
Matching criterion	sum of squared differences (Equation (2))
Reduced basis	see Equation (4)
Interpolant	cubic

2.3 Sensitivity analysis for the selected constitutive laws

For the investigated models, the following sensitivity analysis was performed. First, the macroscopic response in terms of indentation force F_i vs. penetration depth h was computed for the three laws (Figure 5). There is no significant effect of the friction coefficient on the macroscopic response. This observation is in agreement with the results reported by Carlsson et al. [29] and Mostafavi et al. [20]. It was also confirmed by a recent study on the same material [8]. Conversely,

with increasing applied force, the difference between elastic and nonlinear simulations increases. Both nonlinear models lead to the same macroscopic response. This observation is related to the fact that the damage state at the maximum simulated penetration is still very limited in terms of level and region over which it is active (see Section 4). Therefore, the force-penetration response is not affected by introducing damage, which was also reported in Ref. [7].

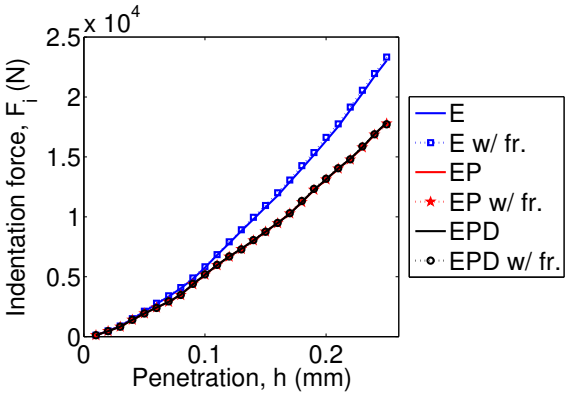

Figure 5: Sensitivity of the indentation depth vs. applied force response for elastic (E), elastoplastic (EP) and Damage (EPD) simulations without and with friction (w/ fr.)

Since DVC analyses used two different ROIs, the same type of analysis was performed for the simulated displacement fields over two different regions. First, the whole DVC ROI (Figure 3) was considered and displacement differences were assessed for *identical* indentation depths. For any comparison, the standard displacement difference (SDD) was computed. For any given constitutive model, the SDD between results with and without friction remains very small (when expressed in voxel, Figure 6(a)). It is therefore expected that it will hardly be detectable via DVC since measurement uncertainties are generally higher than these levels [24]. Conversely, the SDD is larger for nonlinear simulations with respect to elastic calculations, especially for higher indentation depths. The differences between the two nonlinear models remain limited and of the same order of magnitude as for friction.

It was decided to consider a smaller region centered about the indentation point such that $|x| < 1.85$ mm, $|y| < 1.85$ mm, and $-1.85 < z < 0$ mm (see Figure 3). It is referred to as reduced ROI. Overall, the SDDs are higher in the reduced ROI (Figure 6(b)) than in the first ROI (Figure 6(a)). Yet, they remain too small to capture the effect of friction, and possibly that of the two nonlinear models. The reduced ROI is more sensitive for discriminating elastic vs. nonlinear kinematic bases. It will therefore be considered in the following discussions.

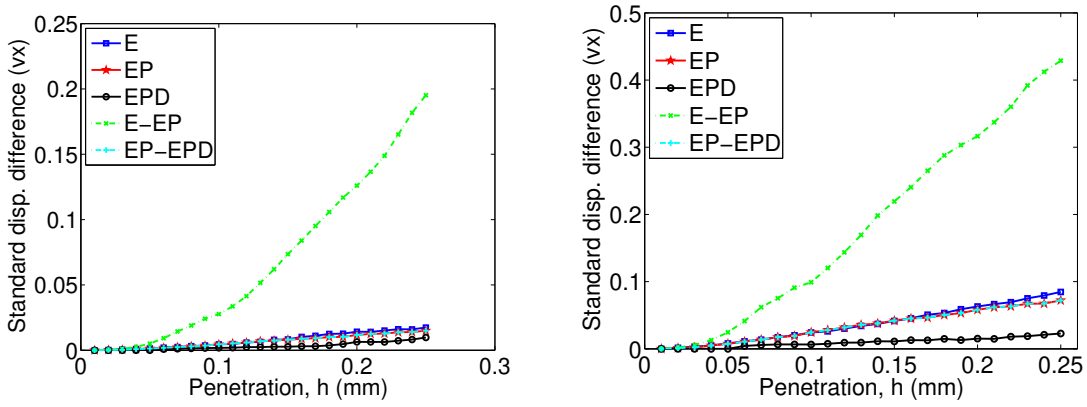

(a) (b)

Figure 6: Sensitivity analysis of displacement differences between elastic analyses (E) with or without friction, elastoplastic analyses (EP) with or without friction, damage analyses (EPD) with or without friction, elastic and elastoplastic simulations (E-EP) with no friction, damage and elastoplastic simulations (EPD-EP) with no friction. Standard displacement differences computed over the whole DVC ROI (a) and the reduced ROI (b). The physical size of one voxel is 30.8 µm

The displacement differences in the axial direction between elastoplastic and elastic predictions are shown in Figure 7. For the first scan, these differences are small (*i.e.,* in the micrometer range) because elasticity was the dominant deformation mechanism even in the reduced ROI. As the applied load increases, the differences between the two models become more pronounced. However their magnitude remains small in comparison with the selected resolution (*i.e.,* 30.8 µm per voxel).

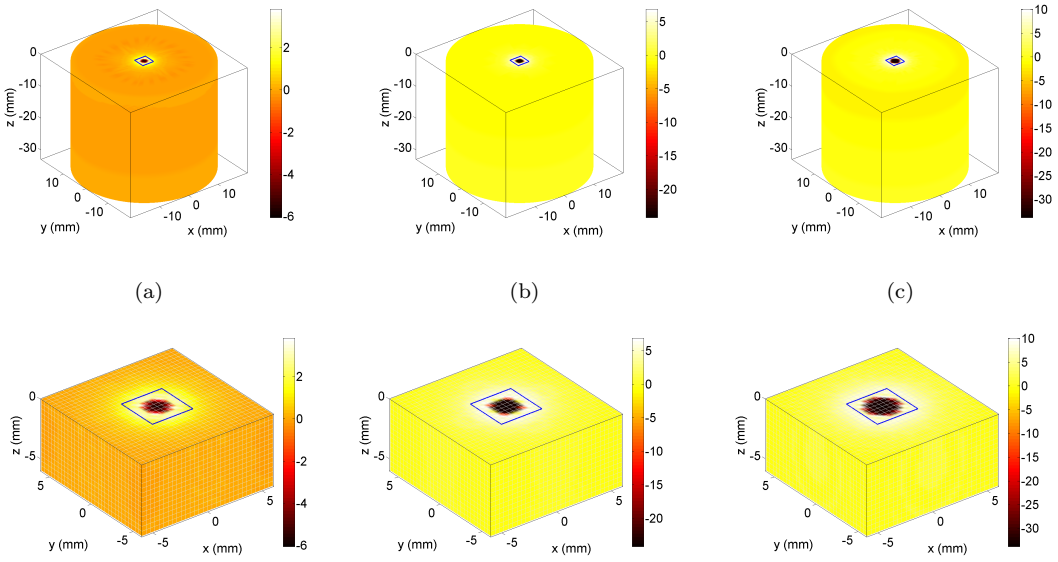

(a) (b) (c)

(d) (e) (f)

Figure 7: Axial displacement differences δu_z (expressed in µm) between the elastoplastic and the elastic models for the three scans. The physical size of one voxel is 30.8 µm. Top row: complete FE model, bottom row: DVC ROI (see Figure 3). The blue boxes depict the reduced ROI. (a) Scan #1, (b) Scan #2, (c) Scan #3

Figure 8 shows the displacement differences in the axial direction between the elastoplastic (EP) and damage (EPD) predictions. Their levels are very small in comparison to the physical size of each voxel. The major differences occur along the periphery of the contact area where damage initiates (Figure 18), which leads to softening that induced these small differences.

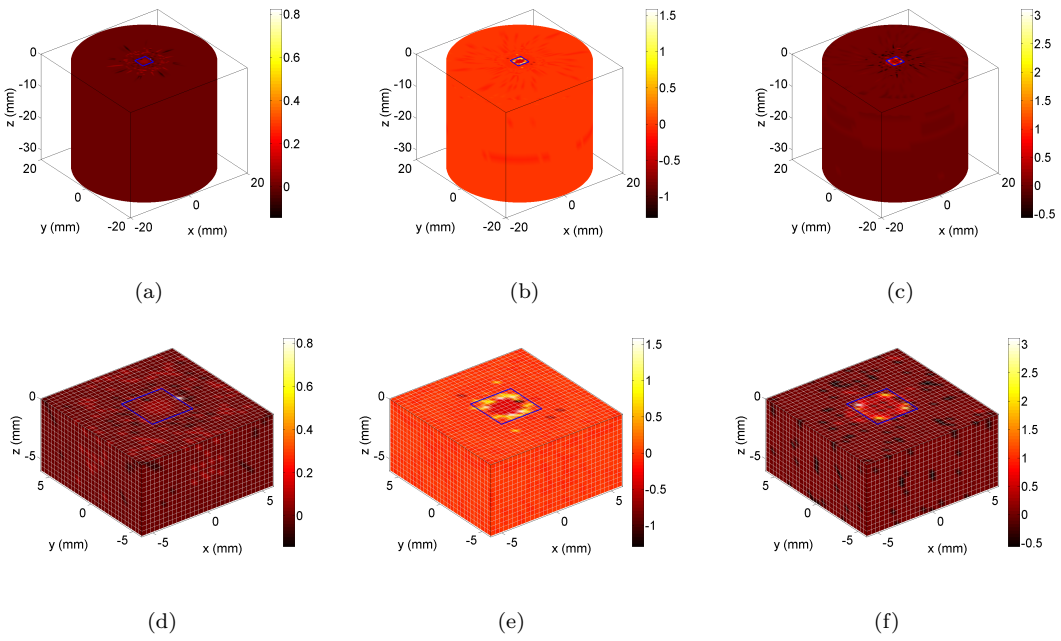

Figure 8: Axial displacement differences δu_z (expressed in µm) bewteen the elastoplastic (EP) and damage (EPD) models for the three scans. The physical size of one voxel is 30.8 µm. Top row: complete FE model, bottom row: DVC ROI (see Figure 3). The blue boxes depict the reduced ROI. (a) Scan #1, (b) Scan #2, (c) Scan #3

3 DVC Results

The DVC analyses were run on the ROI shown in Figure 3. Even though this ROI is less sensitive than the reduced ROI considered in the sensitivity study (Figure 6), it was selected to use more voxels to evaluate the seven degrees of freedom (*i.e.,* $\approx$ 30 Mvx for the DVC ROI vs. 864 kvx for the reduced ROI).

3.1 Elastic (E) analyses

For each scan, DVC analyses were run for different simulated load levels F_i. The root mean square (RMS) gray level residuals were computed over the reduced ROI and are reported in Figure 9. For any analyzed scan, the residuals are sensitive to the selected load levels and minimum levels are clearly observed for all three load levels. As the indentation load is increased, the residuals gradually increase as the proposed solutions describe less precisely the experiment. Conversely, there is virtually no difference between the case with and without friction.

In terms of minimum RMS residual levels (see table in Figure 9), except for the second scan for which the load level is fully consistent with its experimental counterpart, the load levels at minimum residual over-estimate the experimental level. This is particularly true for the third scan

(*i.e.,* the highest indentation force).

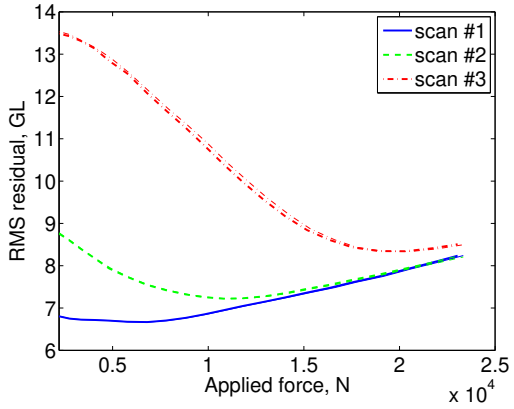

scan #	1	2	3
F_i	5025	10040	15230
$f = 0$	6810	10800	20290
$f = 0.4$	6850	10950	20560

Figure 9: Root Mean Square (RMS) residual as a function of applied force in elastic (E) simulations when $f = 0$ (thick lines) and $f = 0.4$ (thin lines). In the present cases, the results are very close (*i.e.,* the two lines can barely be distinguished). The minimum level for each analyzed case is reported in the table.

One additional piece of information extracted from the DVC analyses is related to the correction factor c for all reported results. As explained in Section 2.2, the closer c to zero, the more faithful the considered model. Figure 10 displays, for all three scans, how the correction factor changes with increasing load. In all cases, there is a unique solution for which $c = 0$, which indicates that the corresponding displacement field is the best with the selected parameters. Interestingly, the load levels for the first two scans are very close to the actual level. Conversely, this is no longer the case for the third scan. All these observations indicate that linear elasticity was not able to properly describe all the physical phenomena involved in the reduced ROI especially for the third scan.

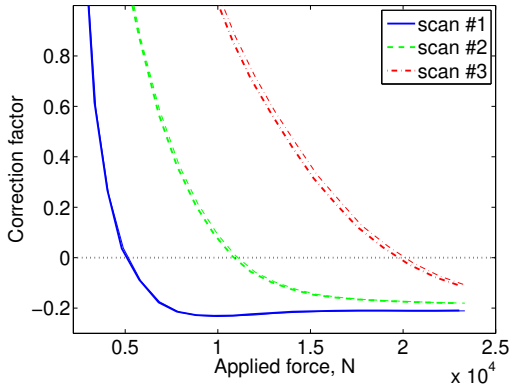

scan #	1	2	3
F_i	5025	10040	15230
$f = 0$	5090	10900	19800
$f = 0.4$	5200	11000	20000

Figure 10: Correction factor c as a function of applied force in elastic (E) simulations when $f = 0$ (thick lines) and $f = 0.4$ (thin lines). The force level when $c = 0$ is reported in the table for each analyzed case.

3.2 Elastoplastic (EP) analyses

The second set of results is related to elastoplastic simulations. Figure 11 shows that the overall trends observed in elastic simulations are equivalent. However, from a quantitative point of view, the minimum levels of RMS residuals were very close to the experimental observation. They still departed for the third scan but not as much as with elastic simulations (Figure 9). The effect of friction was even more limited in the present simulations compared to the previous ones.

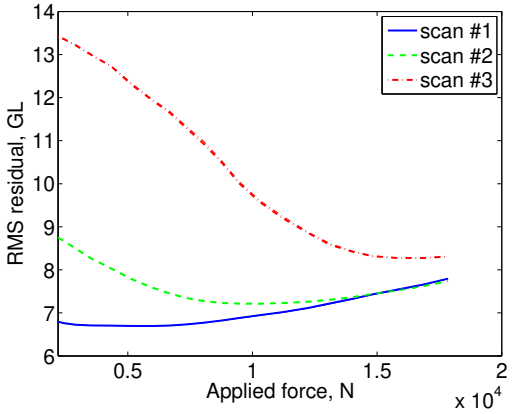

scan #	1	2	3
F_i	5025	10040	15230
$f = 0$	5160	10290	16870
$f = 0.4$	5200	11000	16800

Figure 11: Root Mean Square (RMS) residual as a function of applied force in elastoplastic (EP) simulations when $f = 0$ (thick lines) and $f = 0.4$ (thin lines). The minimum level for each analyzed case is reported in the table.

All the conclusions drawn from the RMS residuals are confirmed by the correction coefficient reported in Figure 12. In particular, the load levels that cancel out the correction factor c were very close to the experimental value except for the third scan.

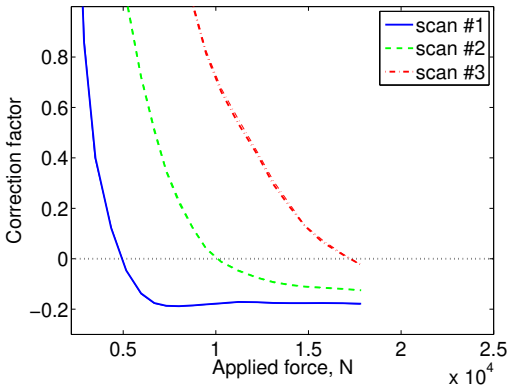

scan #	1	2	3
F_i	5025	10040	15230
$f = 0$	4940	10100	17200
$f = 0.4$	4950	10100	17200

Figure 12: Correction factor c as a function of applied force in elastoplastic (EP) simulations when $f = 0$ (thick lines) and $f = 0.4$ (thin lines). The force level when $c = 0$ is reported in the table for each analyzed case.

Even though the relative sensitivity of the elastic and elastoplastic models was shown to be in the sub-voxel range (Figure 6), the present results show that the elastoplastic model better

captured the kinematics in the reduced ROI. The two complementary quantities, namely, the RMS residuals and the correction factor proved to be very useful for discriminating the two models.

3.3 Damage (EPD) Model

The complete EPD model is now investigated. The minimum RMS residuals (Figure 13) were virtually identical to those observed with the elastoplastic model (Figure 11). This result is due to the fact that the kinematic sensitivity (Figure 8) between the two models was very low (*i.e.*, well below the physical voxel size). The effect of friction was essentially insignificant.

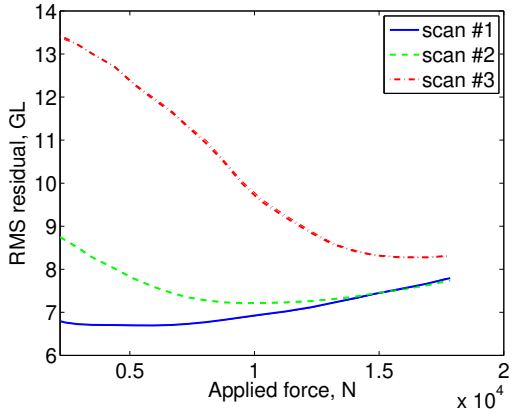

scan #	1	2	3
F_i	5025	10040	15230
$f = 0$	5170	10250	16900
$f = 0.4$	5200	10300	16890

Figure 13: Root Mean Square (RMS) residual as a function of applied force in elastoplastic (EP) simulations when $f = 0$ (thick lines) and $f = 0.4$ (thin lines). The minimum level for each analyzed case is reported in the table.

The correction factors c are reported in Figure 14. When compared to those reported for the elastoplastic model (Figure 12), it is concluded that both models captured in the same way the overall material response beneath the indentor, and that friction did not play a significant role.

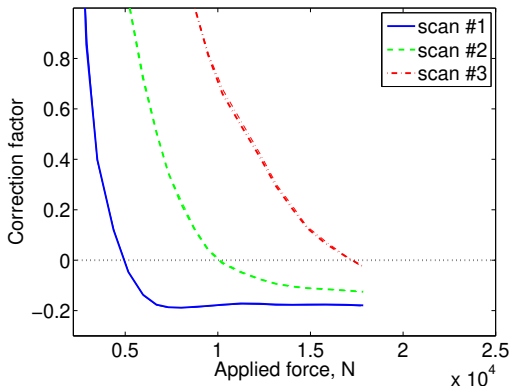

scan #	1	2	3
F_i	5025	10040	15230
$f = 0$	4940	10070	17260
$f = 0.4$	4950	10150	17250

Figure 14: Correction factor c as a function of applied force in elastoplastic (EP) simulations when $f = 0$ (thick lines) and $f = 0.4$ (thin lines). The force level when $c = 0$ is reported in the table for each analyzed case.

4 Discussion

The first set of simulations assumed frictionless contact between the indentor and Bohus granite (*i.e.,* $f = 0$). The RMS residuals and correction factors are gathered in Table 4. For the first load level, all models had the same quality in terms of gray level residuals. This observation was still true for the second scan (with a very slight advantage for the nonlinear models). Conversely, the difference was more significant for the last scan for which the RMS residuals were lower for the two nonlinear models in comparison with the elastic response. The correction factor was also closer to 0 for the nonlinear models. All these observations show that the nonlinear models better captured the deformations beneath the indentor. At this stage, there was no clear difference between the two nonlinear models.

Table 4: Model comparison for the three analyzed scans in terms of RMS gray levels computed over the reduced ROI (ϱ) and correction factor c when $f = 0$

	E		EP		EPD	
scan #	ϱ (GL)	c	ϱ (GL)	c	ϱ (GL)	c
1	6.70	2.5×10^{-3}	6.70	-2.4×10^{-2}	6.70	-2.4×10^{-2}
2	7.25	6.9×10^{-2}	7.21	1.6×10^{-3}	7.21	2×10^{-4}
3	8.82	3.1×10^{-1}	8.29	1.0×10^{-1}	8.29	1.0×10^{-1}

Finite element analyses were also run with a non vanishing friction coefficient ($f = 0.4$). When comparing the results reported in Table 5 with $f = 0.4$ to those of Table 4 (when $f = 0$), it is concluded that the effect of friction was very limited. When nonlinear models were considered, virtually identical results were obtained. This observation is in line with all the previous results and those reported on nano-structured oxide dispersion strengthened steel [20]. It was also numerically observed that the predicted force-penetration response was not affected by frictional effects [8].

Table 5: Model comparison for the three analyzed scans in terms of RMS gray levels computed over the reduced ROI (ϱ) and correction factor c when friction is account for ($f = 0.4$)

	E		EP		EPD	
scan #	ϱ (GL)	c	ϱ (GL)	c	ϱ (GL)	c
1	6.70	1.6×10^{-2}	6.70	-2.4×10^{-2}	6.70	-2.4×10^{-2}
2	7.25	8.7×10^{-2}	7.21	3.5×10^{-3}	7.21	2×10^{-4}
3	8.89	3.4×10^{-1}	8.30	1.0×10^{-1}	8.30	1.0×10^{-1}

In Figure 15, the predicted equivalent plastic strain fields using the EPD model are displayed when the indentation force was equal to 15230 N (*i.e.,* scan #3) and 19850 N (*i.e.,* ultimate load).

The fields are only shown for one half of the DVC ROI (Figure 3). The plastic zone is associated with crushed material due to high pressures under the contact surface as well as shear zones with multiple microcracks. The plastic region extent is similar in both frictionless and frictional cases (*i.e.,* 4 mm in diameter and 3.6 mm in depth for the ultimate load), and consequently the force-penetration response was not significantly affected by frictional effects.

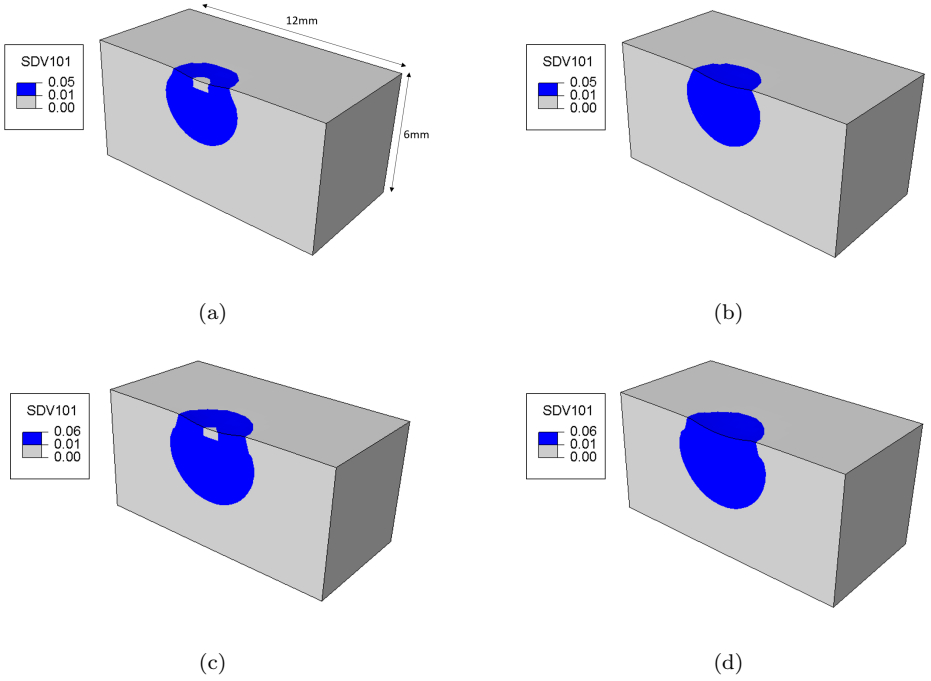

Figure 15: Plastic zones predicted with the EPD model for DVC ROI (see Figure 3). (a) Plastic zones for 15230N when $f = 0$ and (b) when $f = 0.4$. (c) Plastic zones for 19850N when $f = 0$ and (d) when $f = 0.4$.

Figure 16 displays three sections of the last volume (*i.e.,* scan #4), which corresponds to the post-mortem state of indented Bohus granite (Table 1). The dark zones on the upper parts of the sagittal and coronal sections highlight the comminuted material, which underwent inelastic deformations. The extent of the comminuted zone was compared with the predicted plastic zone (yellow circles). A very good correspondence is observed, which further validates the elastoplastic predictions of the two nonlinear models.

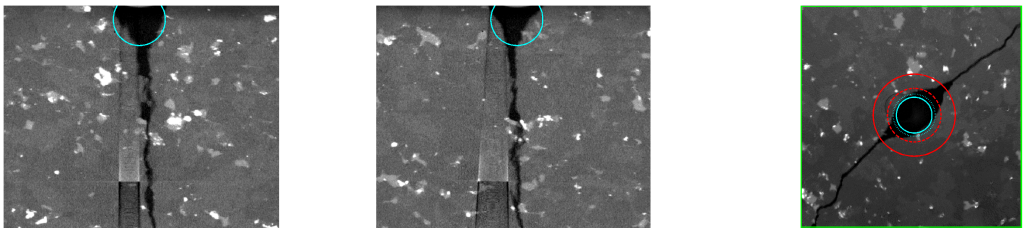

(a) (b) (c)

Figure 16: Post-mortem (scan #4) and predicted comminuted zone. (a) $x-z$ (sagittal), (b) $y-z$ (coronal), (a) $x-y$ (transverse) sections. The cyan circles depict the boundary of the predicted plastic zone (Figure 15). The red circles show the extent of the damage zone (Figure 18) when $f = 0$ (dashed line) and $f = 0.4$ (solid line).

The EPD model enables the initiation probability P_I to be computed using the Weibull parameters (Table 2), which would correspond to the failure probability P_F if the weakest link assumption applied (Appendix B). Figure 17 shows the change of the initiation probability with the indentation force when friction was accounted for or not. Very similar predictions are observed. In the present experiment, the first load drop (green circle in Figure 1) occurred around 9 kN. This level is consistent with the indentation force interval that yields initiation probabilities such that $0 < P_I < 1$ (*i.e.,* $7 < F < 12$ kN).

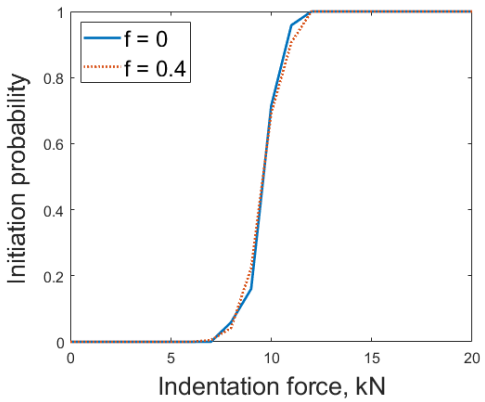

Figure 17: Initiation probability P_I predicted by the EPD model for $f = 0$ and $f = 0.4$.

In the present case, the weakest link assumption did not apply and damage grew beyond the first load drop as the applied load could be doubled prior to final failure (Figure 1(b)). Figure 18 shows damage fields associated with the first principal stress when the indentation force was equal to 15230 N (*i.e.,* scan #3) and 19850 N (*i.e.,* ultimate load). Damage occurred at the periphery of the plastic zone (Figure 15), where the confining stresses were not very high. For this field, there are differences in terms of damaged zone size when friction was accounted for or not. It is

interesting to note the elongated damaged zone along the dominant crack in the simulations, which was also observed experimentally (Figure 16(c)) and in terms of damage extent, the frictional case was closer to the experimental observations.

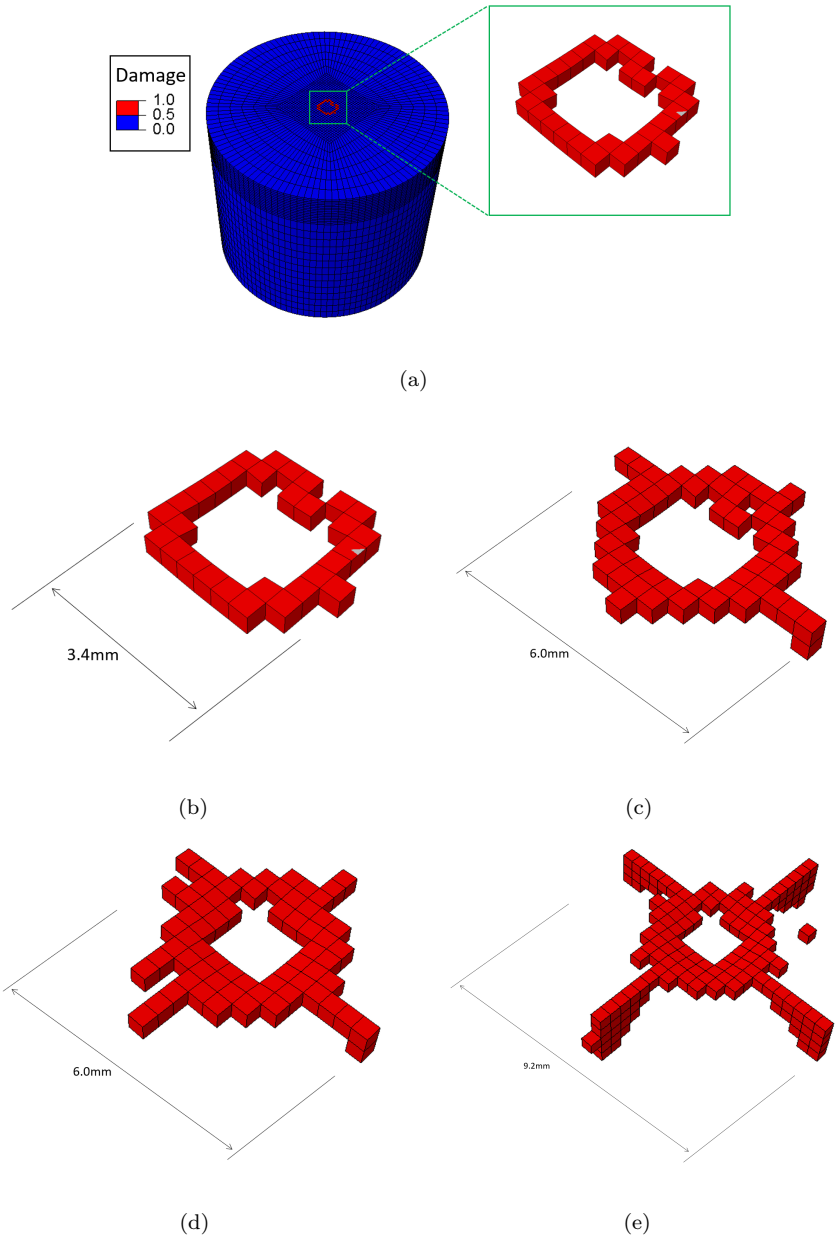

Figure 18: (a) Damage field from FE simulations. (b) Damage fields for 15230N when $f = 0$ and (c) when $f = 0.4$. (d) Damage fields for 19850N when $f = 0$ and (e) when $f = 0.4$.

The EDM model predicted the formation of two splitting cracks. From the experimental observation (Figure 19), it is concluded that one of them propagated earlier than the other one.

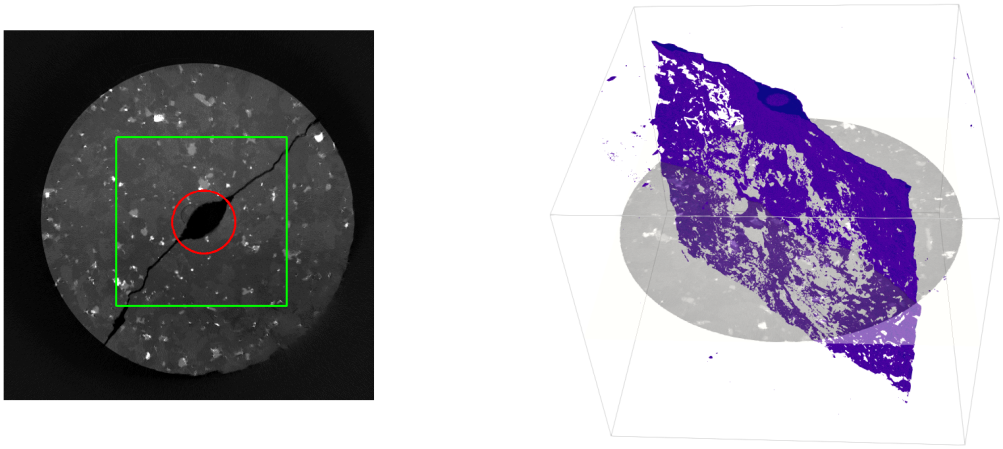

(a) (b)

Figure 19: (a) Top transverse view of the Post-mortem (scan #4) state where one splitting crack eventually led to the fracture of the tested sample. The green box shows the sub-region shown in Figure 16(c). (b) 3D rendering of thresholded scan #4 to reveal the comminuted zone and splitting crack.

5 Conclusion

Spherical indentation of Bohus granite was investigated using Digital Volume Correlation (DVC). The aim was to evaluate the faithfulness of different constitutive laws of the indented granite and the contact properties between the rock and the indentor. A new integrated DVC framework was introduced in which the measured quantities were associated with mechanically admissible (*i.e.,* computed) displacement fields. Each investigated law could be independently probed against global data (*i.e.,* indentation force), its kinematic trustworthiness assessed with the so-called correction parameter associated with simulated displacement fields using meshes with 200 µm long elements, and gray level residuals computed at the voxel scale (*i.e.,* ca. 30 µm). Therefore, three different scales of analyses were covered by such framework.

The most important results concerning the investigated constitutive models are summarized as follows:

- Compressible elastoplasticity should be accounted for to achieve high accuracy in terms of predicted load level *and* displacement fields underneath the indentor. For the latter ones, DVC residuals enabled for the differentiation of linear elastic vs. nonlinear models even though displacement differences remained less than one voxel. Furthermore, the introduced correction factor (further probing the faithfulness of each model) proved very useful in determining the predicted indentation load levels with the selected models.
- Even though the frictional effects between the indentor and the tested granite remained very

limited in terms of plastic zone size and applied load, they led to an extended damage pattern by influencing the corresponding (damage) variables.

- The damage model based on Weibull statistics was able to determine the indentation fracture pattern prior to extensive failure, in addition to the level of first initiation event (*i.e.,* load drop).

Such results are further evidence of the suitability of the coupled elastoplastic/damage model for predicting nonlinear mechanisms that occur in indented hard rocks such as Bohus granite.

Acknowledgments

The authors would like to thank Dr. Kenneth Weddfelt at Epiroc Rock Drills AB for helpful discussions. This work was partially funded by Agence Nationale de la Recherche under grant ANR-10-EQPX-37 (MATMECA) and by Epiroc Rock Drills AB.

Conflict of interest

The authors declare that they have no conflict of interest.

References

[1] D. Tkalich, M. Fourmeau, A. Kane, C.C. Li, and G. Cailletaud. Experimental and numerical study of Kuru granite under confined compression and indentation. *International Journal of Rock Mechanics & Mining Sciences*, 87:55–68, 2016.

[2] J. Lemaitre. *A Course on Damage Mechanics*. Springer-Verlag, Berlin (Germany), 1992.

[3] J. Mazars. A description of microscale and macroscale damage of concrete structures. *Engineering Fracture Mechanics*, 25(5-6):729–737, 1986.

[4] S. Souissi, K. Miled, E. Hamdi, and H. Sellami. Numerical Modeling of Rock Damage during Indentation Process with Reference to Hard Rock Drilling. *International Journal of Geomechanics*, 17, 2017.

[5] H. Shariati, M. Saadati, A. Bouterf, K. Weddfelt, P.L. Larsson, and F. Hild. On the Inelastic Mechanical Behavior of Granite: Study Based on Quasi-oedometric and Indentation Tests. *Rock Mechanics and Rock Engineering*, 52:645–657, 2019.

[6] D.C. Drucker and W. Prager. Soil mechanics and plastic analysis of limit design. *Quat. of Appl. Math.*, 14, 1956.

[7] H. Shariati, M. Saadati, K. Weddfelt, P.-L. Larsson, and F. Hild. A damage model for granite subjected to quasi-static contact loading, 2019.

[8] H. Shariati, M. Saadati, K. Weddfelt, P.-L. Larsson, and F. Hild. Study of frictional effects of granite subjected to quasi-static contact loading. *Lubricants*, 8(12):106, 2020.

[9] E. Maire and P. J. Withers. Quantitative X-ray tomography. *International Materials Reviews*, 59(1):1–43, 2014.

[10] A. Bouterf, S. Roux, F. Hild, J. Adrien, E. Maire, and S. Meille. Digital Volume Correlation Applied to X-ray Tomography Images from Spherical Indentation Tests on Lightweight Gypsum. *Strain*, 50(5):444–453, 2014.

[11] M. Mostafavi, Y. Vertyagina, C. Reinhard, R. Bradley, X. Jiang, M. Galano, and J. Marrow. 3D Studies of Indentation by Combined X-Ray Tomography and Digital Volume Correlation. In *Materials Structure Micromechanics of Fracture VII*, volume 592 of *Key Engineering Materials*, pages 14–21. Trans Tech Publications Ltd, 3 2014.

[12] Y. Vertyagina, M. Mostafavi, C. Reinhard, R. Atwood, and T.J. Marrow. In situ quantitative three-dimensional characterisation of sub-indentation cracking in polycrystalline alumina. *Journal of the European Ceramic Society*, 34(12):3127–3132, 2014.

[13] A. Bouterf, E. Maire, S. Roux, F. Hild, X. Brajer, E. Gouillart, and E. Boller. Analysis of compaction in brittle foam with multiscale indentation tests. *Mechanics of Materials*, 118:22–30, 2018.

[14] X. Lu, M. Peña Fernández, R.S. Bradley, S.D. Rawson, M. O'Brien, B. Hornberger, M. Leibowitz, G. Tozzi, and P.J. Withers. Anisotropic crack propagation and deformation in dentin observed by four-dimensional X-ray nano-computed tomography. *Acta Biomaterialia*, 96:400–411, 2019.

[15] L. Ma, A.-L. Fauchille, M.R. Chandler, P. Dowey, K.G. Taylor, J. Mecklenburgh, and P.D. Lee. In-situ synchrotron characterisation of fracture initiation and propagation in shales during indentation. *Energy*, 215:119161, 2021.

[16] B. Cai, S. Karagadde, T.J. Marrow, T. Connolley, and P.D. Lee. Synchrotron X-ray Tomographic Quantification of Deformation Induced Strain Localisation in Semi-solid Al-15wt.%Cu. *IOP Conference Series: Materials Science and Engineering*, 84:012079, 2015.

[17] B. Cai, P.D. Lee, S. Karagadde, T.J. Marrow, and T. Connolley. Time-resolved synchrotron tomographic quantification of deformation during indentation of an equiaxed semi-solid granular alloy. *Acta Materialia*, 105:338–346, 2016.

[18] L. Saucedo-Mora, M. Mostafavi, D. Khoshkhou, C. Reinhard, R. Atwood, S. Zhao, B. Connolly, and T.J. Marrow. Observation and simulation of indentation damage in a SiC-SiC$_{fibre}$ ceramic matrix composite. *Finite Elements in Analysis and Design*, 110:11–19, 2016.

[19] M. Mostafavi, D.M. Collins, B. Cai, R. Bradley, R.C. Atwood, C. Reinhard, X. Jiang, M. Galano, P.D. Lee, and T.J. Marrow. Yield behavior beneath hardness indentations in ductile metals, measured by three-dimensional computed X-ray tomography and digital volume correlation. *Acta Materialia*, 82:468–482, 2015.

[20] M. Mostafavi, R. Bradley, D.E.J. Armstrong, and T.J. Marrow. Quantifying yield behaviour in metals by X-ray nanotomography. *Scientific Reports*, 6:34346, 2016.

[21] T. Lacondemine, J. Réthoré, E. Maire, F. Célarié, P. Houizot, C. Roux-Langlois, C.M. Schlepütz, and T. Rouxel. Direct observation of the displacement field and microcracking in a glass by means of X-ray tomography during in situ Vickers indentation experiment. *Acta Materialia*, 179:424–433, 2019.

[22] A. Bouterf, J. Adrien, E. Maire, X. Brajer, F. Hild, and S. Roux. Identication of the Crushing Behavior of Brittle Foam: From Indentation to Oedometric Tests. *Journal of the Mechanics and Physics of Solids*, 98:181–200, 2017.

[23] M. Saadati. *On the mechanical behavior of granite: Constitutive modeling and application to percussive drilling.* Doctoral dissertation, KTH Royal Institute of Technology, 2015.

[24] A. Buljac, C. Jailin, A. Mendoza, J. Neggers, T. Taillandier-Thomas, A. Bouterf, B. Smaniotto, F. Hild, and S. Roux. Digital Volume Correlation: Review of Progress and Challenges. *Experimental Mechanics*, 58(5):661–708, 2018.

[25] B.K. Bay. Methods and applications of digital volume correlation. *Journal of Strain Analysis for Engineering Design*, 43:745–760, 2008.

[26] H. Leclerc, J. Neggers, F. Mathieu, F. Hild, and S. Roux. *Correli 3.0.* IDDN.FR.001.520008.000.S.P.2015.000.31500, Agence pour la Protection des Programmes, Paris (France), 2015.

[27] F. Hild, A. Bouterf, L. Chamoin, F. Mathieu, J. Neggers, F. Pled, Z. Tomičević, and S. Roux. Toward 4d mechanical correlation. *Advanced Modeling and Simulation in Engineering Sciences*, 3(1):1–26, 2016.

[28] Abaqus analysis user's manual version 6.14-2, 2014.

[29] S. Carlsson, S. Biwa, and P.-L. Larsson. On frictional effects at inelastic contact between spherical bodies. *International Journal of Mechanical Sciences*, 42(1):107–128, 2000.

[30] C. Denoual and F. Hild. Dynamic fragmentation of brittle solids: A multi-scale model. *European Journal of Mechanics - A/Solids*, 21(1):105–120, 2002.

[31] P. Forquin and F. Hild. A probabilistic damage model of the dynamic fragmentation process in brittle materials. *Adv. Appl. Mech.*, 44:1–72, 2010.

[32] M. Saadati, P. Forquin, K. Weddfelt, P.-L. Larsson, and F. Hild. On the mechanical behavior of granite material with particular emphasis on the influence from pre-existing cracks and defects. *Journal of Testing and Evaluation*, 46(1):33–45, 2017.

[33] M. Saadati, P. Forquin, K. Weddfelt, P.-L. Larsson, and F. Hild. Granite rock fragmentation at percussive drilling - experimental and numerical investigation. *International Journal for Numerical and Analytical Methods in Geomechanics*, 38(8):828–843, 2014.

[34] M. Saadati, P. Forquin, K. Weddfelt, P.-L. Larsson, and F. Hild. A numerical study of the influence from pre-existing cracks on granite rock fragmentation at percussive drilling. *International Journal for Numerical and Analytical Methods in Geomechanics*, 39(5):558–570, 2015.

[35] W. Weibull. A statistical theory of the strength of materials. Technical Report Report 151, Roy. Swed. Inst. Eng. Res., 1939.

[36] M. Abramowitz and I.A. Stegun. *Handbook of Mathematical Functions*. Dover Publications, Inc., New York (USA), 1965.

[37] D.G.S. Davies. The statistical approach to engineering design in ceramics. *Proc. Brit. Ceram. Soc.*, 22:429–452, 1973.

Appendix A: DVC hardware parameters

Tomograph	North Star Imaging X50+
X-ray source	XRayWorX XWT-240-CT
Target / Anode	W (reflection mode)
Filter	none
Voltage	140 kV
Current	220 µA
Focal spot size	5 µm
Tube to detector	938 mm
Tube to object	192 mm
Detector	Dexela 2923
Definition	1536 × 1944 pixels (2 × 2 binning)
Number of projections	1000
Angular amplitude	360°
Frame average	25 per projection
Frame rate	7 fps
Acquisition duration	1 h 24 min
Reconstruction algorithm	filtered back-projection
Gray Levels amplitude	8 bits
Volume size	811 × 808 × 707 voxels (after crop)
Field of view	25 × 25 × 22 mm^3 (after crop)
Image scale	30.8 µm/voxel
Pattern	natural (Figure 2)

Appendix B: Constitutive Laws

In this appendix, the three investigated constitutive models are detailed. The last two models required user defined subroutines to be developed within the explicit version of Abaqus.

Elasticity (E)

Isotropic elasticity is assumed. The Cauchy stress tensor $\boldsymbol{\sigma}$ is related to the elastic strain tensor $\boldsymbol{\epsilon}^e$ by

$$\boldsymbol{\epsilon}^e = \frac{1+\nu}{E}\boldsymbol{\sigma} - \frac{\nu}{E}(\boldsymbol{\sigma} : \mathbf{1})\mathbf{1} \tag{9}$$

where E denotes the Young's modulus, ν the Poisson's ratio, and $\mathbf{1}$ the second order identity tensor. In elasticity, the elastic strain tensor $\boldsymbol{\epsilon}^e$ is equal to the infinitesimal strain tensor $\boldsymbol{\epsilon}$.

Elastoplasticity (EP)

Since the strain levels are assumed to remain small, the strain tensor is additively partitioned into elastic and inelastic parts

$$\boldsymbol{\epsilon} = \boldsymbol{\epsilon}^e + \boldsymbol{\epsilon}^i \tag{10}$$

where $\boldsymbol{\epsilon}^i$ denotes the inelastic strain tensor. The Drucker-Prager [6] yield function F_y reads

$$F_y = q - p\tan(\beta) - d \tag{11}$$

where q is von Mises' equivalent stress, p the hydrostatic pressure (*i.e.,* $p = -1/3(\boldsymbol{\sigma} : \mathbf{1})$), d the cohesion, and β the friction angle.

The flow potential reads

$$G = q - p\tan(\psi) \tag{12}$$

where ψ is the dilation angle [5]

$$\psi = \tan^{-1}\left(\frac{3}{3\frac{\dot{\epsilon}_a^i}{\dot{\epsilon}_v^i} - 1}\right) \tag{13}$$

$\dot{\epsilon}_a^i$ the inelastic axial strain rate, and $\dot{\epsilon}_a^v$ the inelastic volumetric strain rate.

Elastoplasticity Coupled With Damage (EPD)

The previous model essentially describes the behavior in compressive (*i.e.,* confined) states. In the present case, it is activated in the immediate vicinity of the indentation zone [5, 8]. Farther away from this compacted zone, cracks may initiate due to tensile stresses [7]. To describe the early stages of such mechanism, the so-called DFH model is considered [30, 31] and coupled with the previous one. It was already applied in the study of dynamic fragmentation of Bohus granite [33, 34, 8].

An anisotropic damage model is considered. In the principal frame, the compliance tensor of damaged elements becomes

$$[\mathbf{S}^D] = \frac{1}{E}\begin{bmatrix} \frac{1}{1-D_1} & -\nu & -\nu \\ -\nu & \frac{1}{1-D_2} & -\nu \\ -\nu & -\nu & \frac{1}{1-D_3} \end{bmatrix} \tag{14}$$

and the growth law of each damage variable D_i associated with principal stress σ_i reads

$$\frac{d^2}{dt^2}\left(\frac{1}{1-D_i}\frac{dD_i}{dt}\right) = 6S(kC_0)^3\widehat{\lambda}_t(\widetilde{\sigma}_i(t)) \quad \text{if} \quad \sigma_i > 0 \quad \text{and} \quad \frac{d\sigma_i}{dt} > 0 \tag{15}$$

with

$$V_{FE}\widehat{\lambda}_t(\widetilde{\sigma}_i(t)) = \begin{cases} 0 & \text{if} \quad \sigma_i(t) < \sigma_k \\ \max\left(1, V_{\text{FE}}\lambda_0\left(\frac{\widetilde{\sigma}_i(t)}{\sigma_0}\right)^m\right) & \text{otherwise} \end{cases} \tag{16}$$

where $\widetilde{\sigma}_i$ is the i-th effective principal stress (*i.e.*, $\widetilde{\sigma}_i = \sigma_i/(1-D_i)$, with no index summation), V_{FE} the volume of the considered finite element, m and σ_0^m/λ_0 the Weibull parameters [35], C_0 the longitudinal wave speed so that the crack propagation velicity is kC_0 (with $k = 0.38$), and $S = 3.74$ the dimensionless shape parameter of the relaxation zones [34]. The stress σ_k is randomly selected for each finite element as the initiation level for the first crack according to the Weibull model

$$\sigma_k = \sigma_0 \left(-\frac{\log(1-P_k)}{\lambda_0 V_{\mathrm{FE}}} \right)^{1/m} \tag{17}$$

where P_k denotes the initiation probability, which is randomly selected in a uniform distribution ranging from 0 to 1. If the weakest link hypothesis applies, the initiation probability is equal to the cumulative failure probability of the considered element

$$P_F = 1 - \exp\left(-\lambda_0 V_{\mathrm{FE}} \left(\frac{\sigma_k}{\sigma_0} \right)^m \right) \tag{18}$$

and the corresponding mean failure stress becomes

$$\overline{\sigma}_F = \frac{\sigma_0}{(\lambda_0 V_{\mathrm{FE}})^{1/m}} \Gamma\left(1 + \frac{1}{m}\right) \tag{19}$$

where Γ is the Euler function of the second kind [36]. If the failure probability of the whole structure is to be evaluated, the volume V_{FE} of any element has to be replaced by the effective volume V_{eff} [37].